Journal of Thermal Analysis and Calorimetry (2020) 141:1413–1423
https://doi.org/10.1007/s10973-019-09102-x

Synthesis, characterization and catalytic behavior of MFe_2O_4 (M = Ni, Zn and Co) nanoparticles on the thermal decomposition of TKX-50

Ming Zhang[1] · Fengqi Zhao[1] · Yanjing Yang[1] · Hui Li[1] · Hongxu Gao[1] · Ergang Yao[1] · Jiankan Zhang[1] · Ting An[1] · Zhoufeng Jiang[1]

Received: 18 August 2019 / Accepted: 24 November 2019 / Published online: 5 December 2019

Abstract

Bimetallic iron oxides ($NiFe_2O_4$, $ZnFe_2O_4$ and $CoFe_2O_4$) were prepared via the facile solvothermal method and characterized using SEM, TEM, XRD, FTIR, XPS and BET instruments. The catalytic behavior of the bimetallic iron oxides on the thermal decomposition of 5, 5′-bistetrazole-1, 1′-diolate (TKX-50) was studied using DSC and TG-DTG methods. Besides, the corresponding kinetic parameters of TKX-50 thermal decomposition were calculated by multi-kinetics methods including traditional, iso-conversional and iteration methods. The thermal decomposition peak temperature (T_p) and the activation energy (E_a) reduced obviously after the addition of bimetallic iron oxides. Among different bimetallic iron oxides, the $ZnFe_2O_4$ has the best catalytic activity for TKX-50 thermal decomposition. The high thermal decomposition peak temperature (T_{HDP}) and average apparent activation energy (E_a) of TKX-50 were decreased by 47.0 °C and 34.34 kJ mol^{-1} in the presence of $ZnFe_2O_4$ sample. The excellent catalytic activity of $ZnFe_2O_4$ for thermal decomposition of TKX-50 makes it a promising combustion catalyst of insensitive solid propellants containing TKX-50.

Keywords Bimetallic iron oxide · Thermal decomposition · TKX-50 · Catalysis

Introduction

The development of energetic materials is of great significance from the military to civil aspects [1, 2]. As the energy component of explosive and propellant, the performances of the energetic compounds have great influence on the operational efficiency and survivability of missile weapons [3–6]. Therefore, it is of great interest to synthesize energetic materials with both high energy and low sensitivity [7, 8]. The synthesized 5, 5′-bistetrazole-1, 1′-diolate (TKX-50) has attracted extensive attention not only owing to its high theoretical density (1.918 g cm^{-3}), detonation velocity (9679 M s^{-1}) and detonation pressure (42.4 MPa), but also to its low friction and impact sensitivity even lower than that of the traditional explosives octahydro-1,3,5,7-tetranitro-1,3,5,7-tetrazocine (HMX) and hexahydro-1,3,5-trinitro-1,3,5-triazine (RDX) [9–13]. TKX-50 used in solid propellant can not only improve the energetic performance, but also avoid the potential risks caused by the introduction of highly sensitive energetic compounds [9].

Additionally, TKX-50 burns faster than HMX and approaches the burning rate of 2,4,6,8,10,12-hexanitro-2,4,6,8,10,12-hexaazaisowurtzitane (CL-20), which owns excellent application prospect in the field of solid propellants [10]. The thermal decomposition property of energetic component has a critical influence on the combustion performance of solid propellant [11–13]. Differential scanning calorimetry (DSC) and thermogravimetric (TG) methods are usually used methods for the investigation of thermal decomposition properties of energetic materials [14]. Besides, the kinetic parameters including apparent activation energies and Arrhenius parameters calculated using DSC or TG-DTG data play the important role on the understanding of thermal decomposition of energetic component [15]. Trache et al. [16]. studied the thermal decomposition performance and kinetic parameters using

Electronic supplementary material The online version of this article (https://doi.org/10.1007/s10973-019-09102-x) contains supplementary material, which is available to authorized users.

✉ Fengqi Zhao
npecc@21cn.com

[1] Science and Technology on Combustion and Explosion Laboratory, Xi'an Modern Chemistry Research Institute, Xi'an, 710065, China

iso-conversional models, which better reflect the decomposition process than traditional liner methods.

The thermal decomposition performance of pristine TKX-50 was studied, and the kinetic parameters of TKX-50 were calculated using iso-conversional Friedman and Vyazovkin methods [17]. Additionally, the combustion catalyst plays an essential role in the thermal decomposition and combustion performance regulation of solid propellant although its tiny addition amounts [18]. However, most of the published studies involved only experimental and theoretical studies of pristine TKX-50 [17, 18]. It is vital to study the catalytic effects of combustion catalysts (transition metal oxide) on the thermal decomposition of TKX-50 [19–22]. In our preliminary study, the excellent catalytic activity of iron for thermal decomposition of energetic ionic salts including TKX-50 were illustrated [23, 24].

Therefore, three kinds of bimetallic iron oxides ($NiFe_2O_4$, $ZnFe_2O_4$ and $CoFe_2O_4$) and iron oxide were prepared and used for thermal decomposition of TKX-50 in the present work. The morphology, size and composition of the bimetallic iron oxides were characterized using SEM, TEM, XRD, FTIR, BET and XPS instruments. The catalytic action of different iron containing catalysts for TKX-50 thermal decomposition was characterized by means of DSC and TG-DTG. The kinetic parameters for thermal decomposition of TKX-50 were calculated using multi-kinetics methods including traditional, iso-conversional and iteration methods. Based on the above studies, the catalytic performance of various iron containing catalysts for TKX-50 thermal decomposition was analyzed (see Fig. 1).

Experimental

Materials

All the chemicals used were of analytical grade and used without further purification. Ferric nitrate hydrate ($Fe(NO_3)_3{\cdot}9H_2O$), ferric trichloride hexahydrate ($FeCl_3{\cdot}6H_2O$), nickel chloride hexahydrate ($NiCl_2{\cdot}6H_2O$), zinc chloride ($ZnCl_2$), cobalt chloride hexahydrate ($CoCl_2{\cdot}6H_2O$), sodium acetate and polyethylene glycol (Mn = 4000) were purchased from Aladdin Inc. Ethylene glycol (Sinopharm Chemical Reagent Co., Ltd.), ethanol (EA) (Xi'an Chemical Reagent Factory) and distilled water were used for the sample preparation and treatment. Ammonia (FuYu Chemical Co., Ltd. of TianJin, 25%) was used to adjust pH value. TKX-50 with purity higher than 99.5% was obtained from Xi'an Modern Chemistry Research Institute.

Preparation of MFe_2O_4 (M = Ni, Zn and Co)

Certain amounts of $FeCl_3{\cdot}6H_2O$ (5 mmol) was dissolved and mixed with $NiCl_2{\cdot}6H_2O$, $ZnCl_2$ and $CoCl_2{\cdot}6H_2O$ (2.5 mmol) in 60 mL ethylene glycol under magnetic agitation, respectively. Then, sodium acetate (3.6 g) and polyethylene glycol (1.0 g) were added to the above three solutions and mixed homogeneous. The reactants were transformed into 100 mL Teflon-sealed autoclave and heated at 180 °C for 24 h. After cooling, the products were washed several times by distilled water and absolute alcohol and cured at 60 °C in a vacuum oven over night. The obtained powder was ground for further characterization. The yields of the $NiFe_2O_4$, $CoFe_2O_4$ and $ZnFe_2O_4$ are 76%, 77% and 79%, respectively. Besides, the

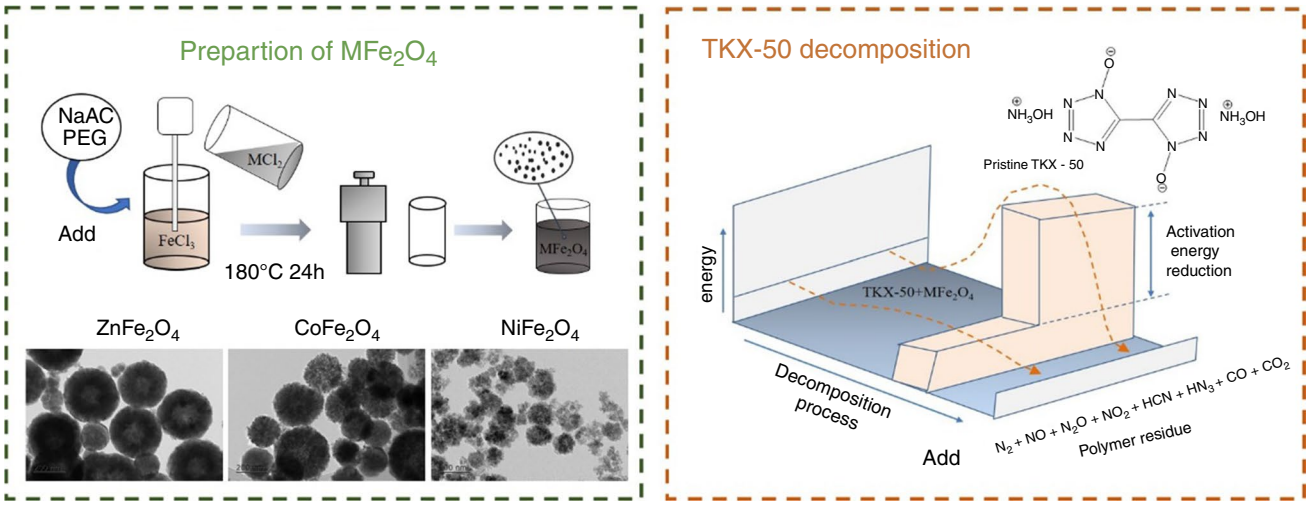

Fig. 1 Illustration of the MFe_2O_4 fabrication and the catalytic mechanism for TKX-50 thermal decomposition

preparation method of Fe_2O_3 refers to our previous published literature [24].

Characterization

The morphology and size of Fe_2O_3 and MFe_2O_4 (M = Ni, Zn and Co) were characterized by scanning electron microscope (SEM, Quanta600, Quantachrome, America) and transmission electron microscopy (TEM, Tecnai G2 F20, FEI, America). The structure and composition were analyzed using X-ray diffraction (XRD, Empyrean, PANalytical, Netherlands), Fourier transform infrared spectroscopy (FTIR, Tensor 27, Bruker, Germany) and X-ray photoelectron spectroscopy (XPS, NEXSA, Thermo scientific, Britain) instruments. XRD was collected with Cu Kα source in the measurement angle range of $2\theta = 5°$–$90°$ with a scan rate of $8°\ min^{-1}$. The specific surface area of Fe_2O_3 and MFe_2O_4 (M = Ni, Zn and Co) samples was characterized using BET (JW-BK112, China). The catalytic action of Fe_2O_3 and MFe_2O_4 samples on thermal decomposition of TKX-50 (the mass ratio of the catalysts in the TKX-50-based composites is 1/11) were studied by differential scanning calorimeter (DSC, 200 F3, NETZSCH, Germany) with a heating rate of 5, 10, 15 and 20 °C min^{-1}, respectively (N_2 flow rate of 50 mL min^{-1}, sample mass of 0.5 ± 0.2 mg). TG-DTG (Netzsch STA 449C with TASC 414/4 controller, Germany) with a heating rate of 10 °C min^{-1} (Ar flow rate of 50 mL min^{-1}, sample mass of 1.0 ± 0.2 mg) was studied.

Kinetics calculation

The traditional Kissinger (Eq. 1), Ozawa (Eq. 2), Flynn–Wall–Ozawa (FWO, Eq. 3) [25] and nonlinear isoconversional Kissinger (Eq. 4) and Ozawa (Eq. 5) iterative methods were employed to obtain the kinetic parameters of TKX-50, respectively [24].

$$\ln\left(\frac{\beta}{T^2}\right) = \ln\frac{AR}{E} - \frac{E}{RT} \tag{1}$$

$$Lg(\beta) = C - \frac{0.4567E}{RT} \tag{2}$$

$$\lg\beta = \lg\left(\frac{AE}{RF(\alpha)}\right) - 2.315 - 0.4567\frac{E}{RT} \tag{3}$$

$$\ln\left(\frac{\beta}{Q_4(u)T^2}\right) = \ln\left(\frac{AR}{EG(\alpha)}\right) - \frac{E}{RT} \tag{4}$$

$$\ln\left(\frac{\beta}{H(u)}\right) = \ln\frac{0.00484AE}{RG(\alpha)} - \frac{1.0516E}{RT} \tag{5}$$

Here, E is activation energy (J mol^{-1}), T is temperature (K), β is heating rate (K min^{-1}), R is universal gas constant (8.314 J mol^{-1} K^{-1}), A is pre-exponential factor (s^{-1}), and the functions in the formula (4) and (5) are expressed as Eqs. (6)–(10).

$$Q_4(u) = \frac{u^4 + 18u^3 + 86u^2 + 96u}{u^4 + 20u^3 + 120u^2 + 240u + 120} \tag{6}$$

$$H(u) = \frac{e^{-u}Q_4(u)/u^2}{0.00484e^{-1.0516u}} \tag{7}$$

$$u = \frac{E}{RT} \tag{8}$$

$$G(\alpha) = \frac{AE}{\beta R}0.00484e^{-1.0516u}H(u) \tag{9}$$

Compared with the traditional methods, the activation energy (iteration calculation until $E_i - E_{i-1} < 0.1$ kJ mol^{-1}) calculated by the nonlinear iso-conversional iteration methods is more reasonable.

Results and discussion

Morphology and composition characterization

Morphology and size

The morphology and size of MFe_2O_4 (M = Ni, Zn and Co) samples were characterized using SEM and TEM, and the results are shown in Fig. 2. SEM images showed that the MFe_2O_4 (M = Ni, Zn and Co) samples exhibit spherical morphology with a uniform size distribution. As can be seen from Fig. 2a–c, $NiFe_2O_4$, $ZnFe_2O_4$ and $CoFe_2O_4$ samples present rough surface with particle size about 70 nm, 360 nm and 220 nm, respectively.

TEM results (Fig. 2d–f) indicated that the MFe_2O_4 (M = Ni, Zn and Co) were composed of agglomerated hollow particles, which are consistent with the rough surface shown in SEM images. The HRTEM images of the $NiFe_2O_4$, $ZnFe_2O_4$ and $CoFe_2O_4$ (Fig. 2g–i) showed clear lattice fringes with the inter-planar distance of 0.250, 0.247 and 0.248 nm, respectively, which can be indexed to the (311) plane of the cubic structure. In addition, the BET results indicated that the specific surface area of $NiFe_2O_4$, $ZnFe_2O_4$, $CoFe_2O_4$ and Fe_2O_3 samples are 105.1, 34.68, 42.07 and 21.26 $m^2\ g^{-1}$, respectively. The BET results are consistent well with the results of SEM and TEM, that is, smaller particle size possess lager specific surface area.

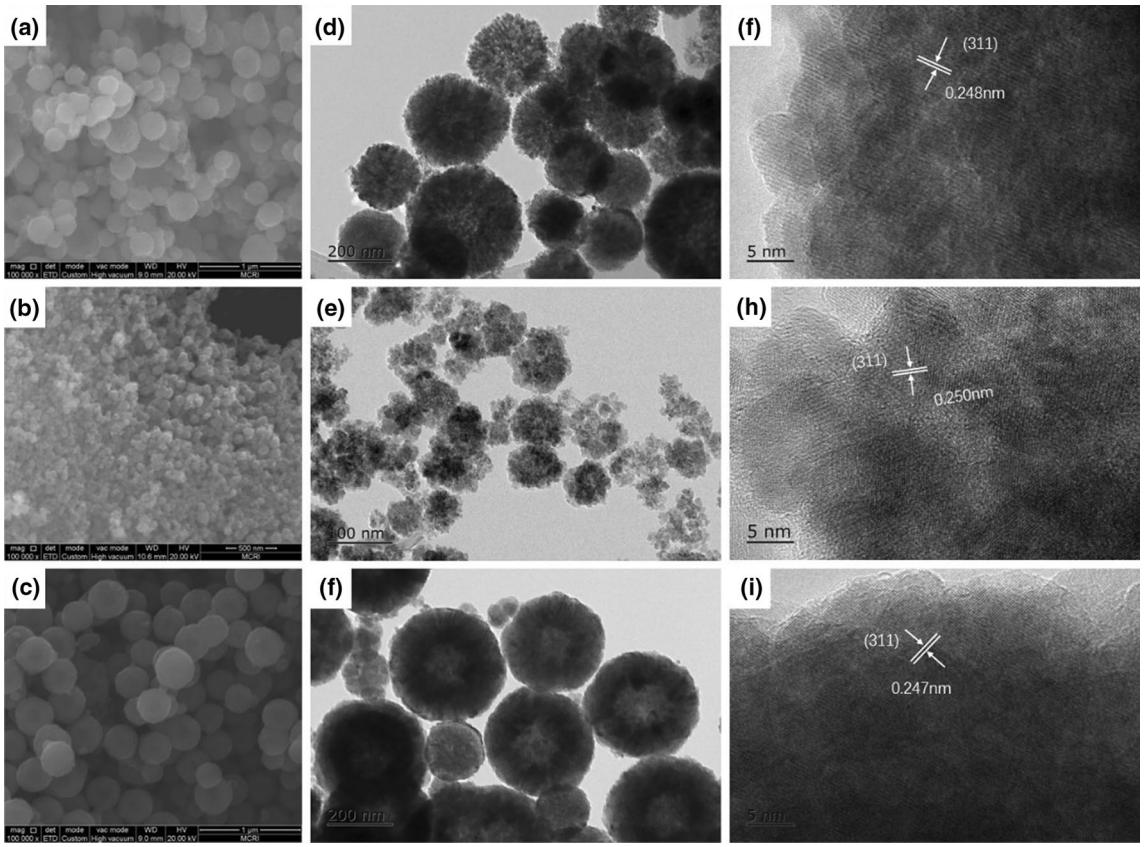

Fig. 2 SEM (**a**–**c**), TEM (**d**–**f**) and HRTEM (**g**–**i**) images of $CoFe_2O_4$ (**a**, **d**, **g**), $NiFe_2O_4$ (**b**, **e**, **h**) and $ZnFe_2O_4$ (**c**, **f**, **i**) and Fe_2O_3 samples

Composition and structure

The crystalline structure and composition of the as-synthesized MFe_2O_4 (M = Ni, Zn and Co) and Fe_2O_3 samples were characterized by XRD, and the patterns are presented in Fig. 3. The XRD patterns of $CoFe_2O_4$ at 18.2°, 30.0°, 35.4°, 37.0°, 43.0°, 53.4°, 56.9°, 62.5° and 74.0° can be indexed to (111), (220), (311), (222), (400), (422), (511), (440) and (533) of cobalt iron oxide (JCPDS No. 22-1086). The diffraction peaks shown in $NiFe_2O_4$ and $ZnFe_2O_4$ patterns correspond well with the crystal planes of (111), (220), (311), (222), (400), (422), (511), (440) and (533) planes of trevorite (JCPDS No. 54-0964) and franklinite (JCPDS No. 22-1012), respectively. The XRD patterns demonstrate the successful fabrication of MFe_2O_4 (M = Ni, Zn and Co) via the solvothermal process. As regards the other impurity phases, no diffraction peaks were observed, which is also indicative of the high purity of the synthesized MFe_2O_4 (M = Ni, Zn and Co). Besides, the average crystallite size of MFe_2O_4 (M = Ni, Zn and Co) was calculated using Scherrer's equation, and the average crystallite size of $NiFe_2O_4$, $ZnFe_2O_4$ and $CoFe_2O_4$ samples are 13.17, 26.16 and 18.14 nm, respectively.

FTIR measurement was also used to investigate the composition of Fe_2O_3 and MFe_2O_4 (M = Ni, Zn and Co), and the corresponding spectra are shown in Fig. 4. The absorption peaks of MFe_2O_4 appear around 3420 cm^{-1} and 1625 cm^{-1},

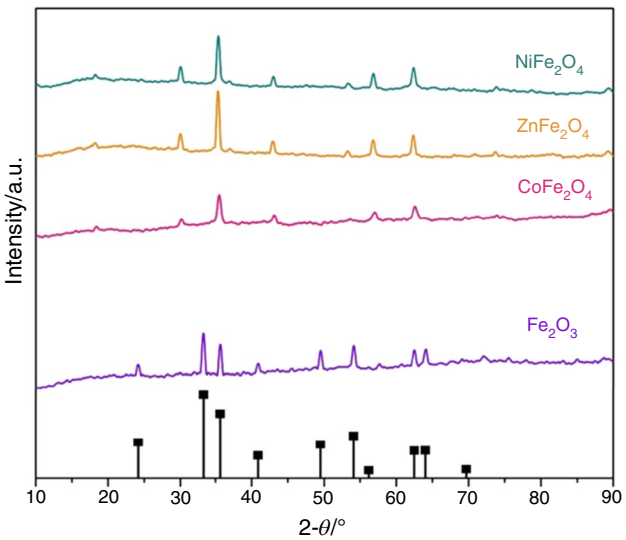

Fig. 3 XRD results of $NiFe_2O_4$, $ZnFe_2O_4$, $CoFe_2O_4$ and Fe_2O_3 samples

which can be derived from the O–H stretching vibration and bending vibration of adsorbed water molecules, respectively. For Fe_2O_3 samples, strong peaks of Fe–O at 564 and 477 cm^{-1} appeared in the Fe_2O_3 sample, which are consisted well with the previous study [23]. Moreover, for MFe_2O_4 (M = Ni, Zn and Co) samples, two strong absorption peaks at lower frequency (around 550 and 415 cm^{-1}) can be assigned to the stretching vibrations of the M–O bonds in tetrahedral positions and the Fe–O bonds in octahedral positions, respectively [26]. Additionally, peaks around 1400, 1050 and 800 cm^{-1} appear in MFe_2O_4 samples, which can be assigned to the deformation vibrations of C–OH, stretching vibrations of C–O and the bending vibration of C–H bonds, respectively [26]. These functional groups are derived from the polyethylene glycol, which is used as surfactant for dispersion.

XPS was carried out to study the elemental composition and chemical state of MFe_2O_4 (M = Ni, Zn and Co) samples, and the results are shown in Fig. 5. The wide scan XPS confirmed the existence of C, O and Fe elements in all MFe_2O_4 samples. Besides, Ni, Zn and Co elements have also been confirmed to exist separately in $NiFe_2O_4$, $ZnFe_2O_4$ and $CoFe_2O_4$ samples, and no other hetero-elements are detected. The peaks around 711, 719.0 and 725 eV in $CoFe_2O_4$, $NiFe_2O_4$ and $ZnFe_2O_4$ samples are related to Fe $2p_{3/2}$, satellite peak and Fe $2p_{1/2}$, providing clear evidence for the existence of Fe^{3+} [27]. For $CoFe_2O_4$ sample, two peaks located at 780.9and 796.6 eV can be assigned to the spectra of Co $2p_{3/2}$ and Co $2p_{1/2}$ of Co^{2+} [28]. Peaks at 856.0 and 873.8 eV are related to the Ni $2p_{3/2}$ and Ni $2p_{1/2}$ spectra of Ni^{2+} in $NiFe_2O_4$ sample [29]. For $ZnFe_2O_4$ sample, two peaks at 1021.8 and 1044.8 eV can be assigned to the spectra of Zn $2p_{3/2}$ and Zn $2p_{1/2}$ of Zn^{2+}, respectively [30].

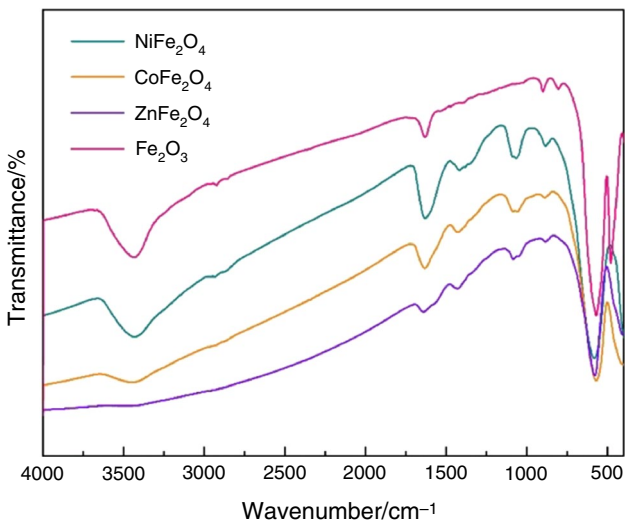

Fig. 4 FTIR spectra of $NiFe_2O_4$, $ZnFe_2O_4$, $CoFe_2O_4$ and Fe_2O_3 samples

The appearance of Co^{2+}, Ni^{2+} and Zn^{2+} peaks separation in $CoFe_2O_4$, $NiFe_2O_4$ and $ZnFe_2O_4$ also confirmed the successful fabrication of MFe_2O_4 (M = Ni, Zn and Co) samples.

Catalytic performance characterization

DSC analysis

DSC curves of TKX-50 before and after mixed with different catalysts are shown in Fig. 6, and the corresponding decomposition peak temperatures and heat released are listed in Table S1. The results indicated that the low thermal decomposition peak temperature (T_{LDP}) and T_{HDP} of TKX-50 reduced obviously after being mixed with $NiFe_2O_4$, $ZnFe_2O_4$ and $CoFe_2O_4$ samples. The T_{LDP} of TKX-50 mixed with $NiFe_2O_4$, $ZnFe_2O_4$ and $CoFe_2O_4$ samples are 210.6, 201.9 and 200.7 °C, respectively, and decreased by 29.3, 38.0 and 39.2 °C in comparison with the T_{LDP} of pristine TKX-50 (239.9 °C) at 10 °C min^{-1}. Additionally, the T_{HDP} of TKX-50 mixed with $NiFe_2O_4$, $ZnFe_2O_4$ and $CoFe_2O_4$ samples are decreased by 39.9, 47.0 and 51.2 °C in comparison with the T_{HDP} of pristine TKX-50 (268.0 °C) at 10 °C min^{-1}. The advanced peak temperature of TKX-50 showed the excellent catalytic performance of bimetallic iron oxides. Besides, the MFe_2O_4 (M = Zn and Co) samples have better effects for the reduction of decomposition temperature than Fe_2O_3, while the $NiFe_2O_4$ has similar effect to Fe_2O_3 sample. The enhancement of the heat generated during TKX-50 pyrolysis also confirmed the catalytic activity of bimetallic iron oxide for TKX-50 thermal decomposition.

TG-DTG analysis

The TG and the corresponding DTG curves of TKX-50, before and after mixing with Fe_2O_3 and MFe_2O_4 (M = Ni, Zn and Co), at the heating rate of 10 K min^{-1} are shown in Fig. 6. The decomposition process of pristine TKX-50 can be divided into two stages [31, 32]. The TG results indicated that the mass loss of pristine TKX-50 after the first decomposition process is 81.80%, and the total mass loss until 450 °C is 95.20%. After mixed with combustion catalysts, the residual mass of TKX-50 is shown in Fig. 6b. As shown in Fig. 6b, the less residue mass of TKX-50 confirms the excellent catalytic of $ZnFe_2O_4$ and $CoFe_2O_4$ samples. Additionally, the DTG peak temperatures decreased to the maximum degree indicating the excellent catalytic activity of $ZnFe_2O_4$ and $CoFe_2O_4$ for TKX-50 thermal decomposition. The results of TG-DTG and DSC are consistent, that is, $CoFe_2O_4$ and $ZnFe_2O_4$ have better catalytic effects than $NiFe_2O_4$ and Fe_2O_3 samples for TKX-50 thermal decomposition.

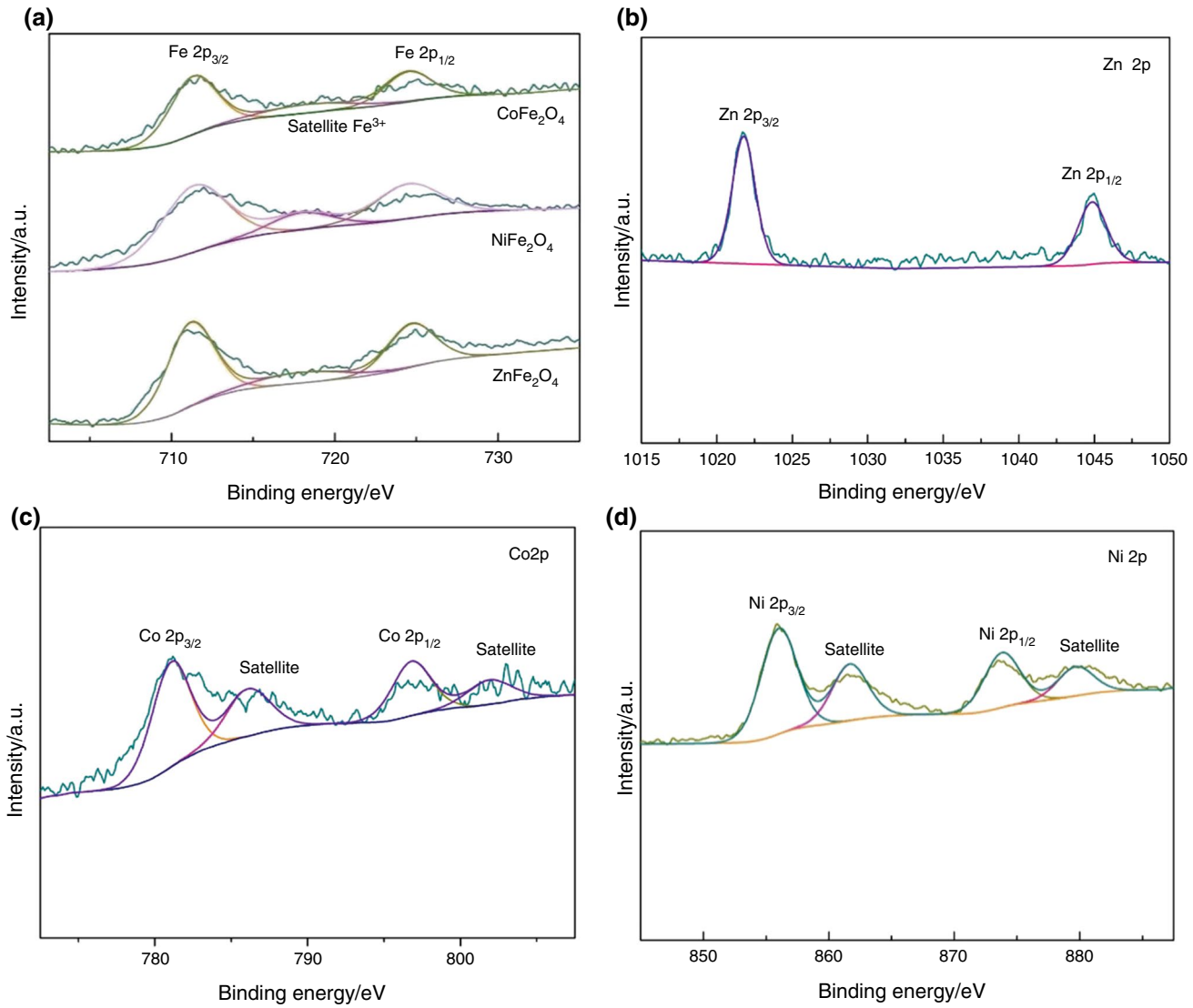

Fig. 5 XPS results of MFe_2O_4 (M = Ni, Zn and Co) samples. **a** Fe 2*p* spectrum of MFe_2O_4 (M = Ni, Zn and Co) samples, **b** Zn 2*p* spectrum of $ZnFe_2O_4$, **c** Co 2*p* spectrum of $CoFe_2O_4$, **d** Ni 2*p* spectrum of $NiFe_2O_4$

Kinetic analysis

Traditional liner Kissinger and Ozawa methods

The apparent activation energy (E_a), pre-exponential factor (Lg*A*) and correlation coefficent (*r*) for the first and high thermal decomposition process of pristine TKX-50 and TKX-50 mixed with Fe_2O_3, $ZnFe_2O_4$, $CoFe_2O_4$ and $NiFe_2O_4$ were evaluated by traditional Kissinger and Ozawa methods. The kinetics data were calculated using thermal decomposition peak temperature (T_p, shown in Table S1 and Fig. S1) at different heating rates (5, 10, 15 and 20 °C min^{-1}), and the corresponding kinetic parameters are shown in Table S2. The results indicated that the E_a of the low temperature decomposition process of TKX-50+Fe_2O_3, TKX-50+$ZnFe_2O_4$, TKX-50+$CoFe_2O_4$ and TKX-50+$NiFe_2O_4$ samples are 168.70, 141.94 and 147.41, 156.66 kJ mol^{-1} respectively, which are decreased by 6.45, 33.21, 28.04 and 18.79 kJ mol^{-1} in comparison with the E_a of pristine TKX-50. Among different catalysts, the activation energies of TKX-50 decrease to the maximum degree demonstrating the excellent catalytic performance of $ZnFe_2O_4$, while the activation energies of pristine TKX-50 calculated using traditional Kissinger and Ozawa methods could not explained the high temperature decomposition process owing to the high error bars and low linearly dependent coefficient (*r*).

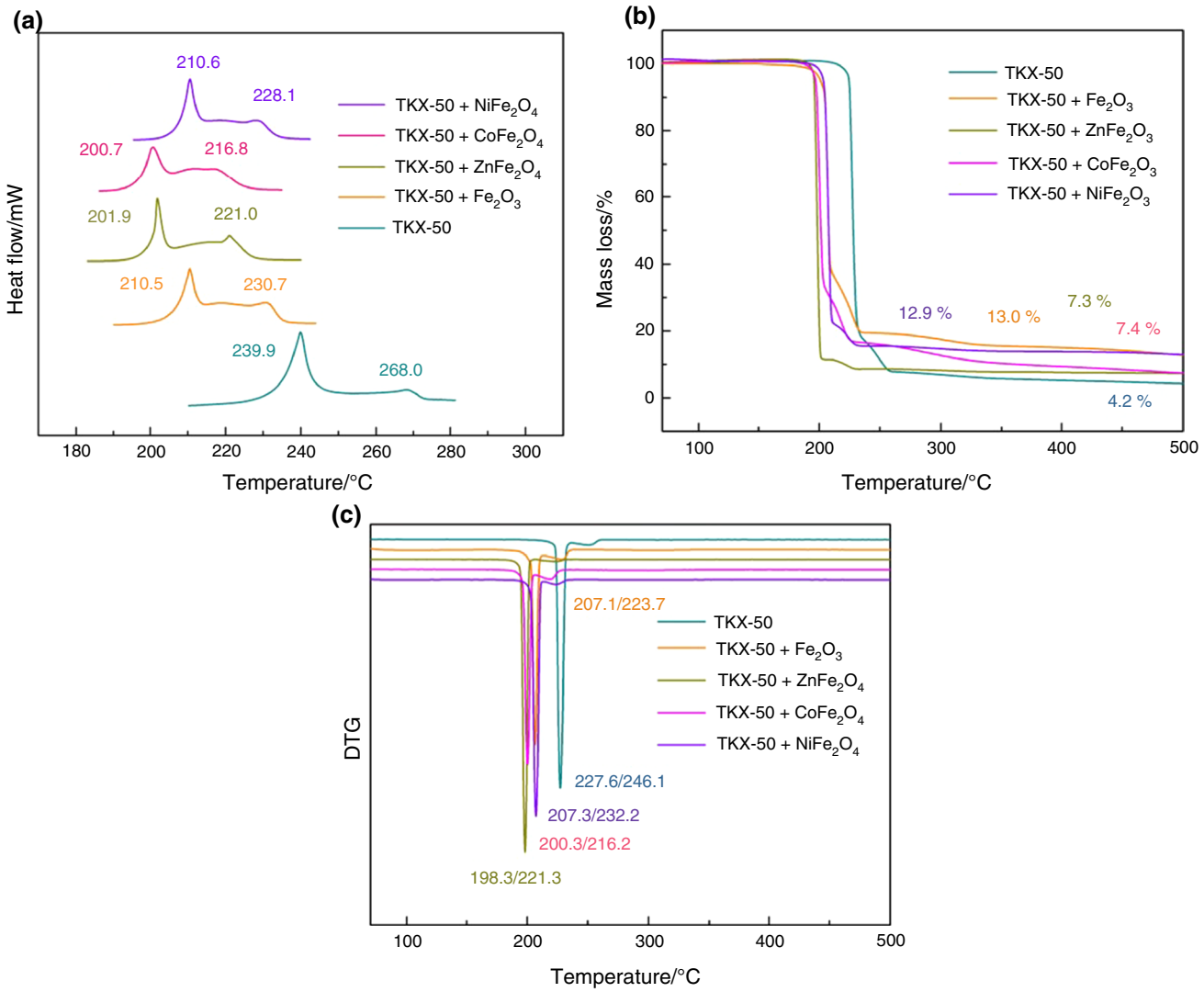

Fig. 6 DSC and TG-DTG curves of TKX-50 before and after being mixed with different catalysts at 10 °C min^{-1}. **a** DSC curves, **b** TG curves, **c** DTG curves

Thus, the iso-conversional and iteration methods were used to calculate the Arrhenius parameters of TKX-50 before and after mixed catalysts.

Iso-conversional methods

The kinetic parameters of TKX-50 calculated using iso-conversional Flynn–Wall–Ozawa method are shown in Fig. 7 and Table 1. The results showed that the activation energy of TKX-50 thermal decomposition reduced obviously after the addition of catalysts. Besides, bimetallic iron oxides own better catalytic effects for the reduction of activation energies of TKX-50, which can be attributed to the synergistic effects between different metals. Besides, the activation energies (conversion degree between 0.3 and 0.8) of TKX-50, before and after mixing with catalysts, are calculated and shown in Table 2. As shown in Table 2, the activation energies of TKX-50 decreased to the max degree after the addition of $ZnFe_2O_4$, indicating the excellent catalytic performance of $ZnFe_2O_4$.

Iteration Kissinger and Ozawa methods

Besides, the apparent activation energies were also calculated using iso-conversional iteration Kissinger and Ozawa methods, and the calculated results are shown in Fig. 8 (the corresponding Arrhenius parameters are shown in Table S2 and S3). The activation energies calculated

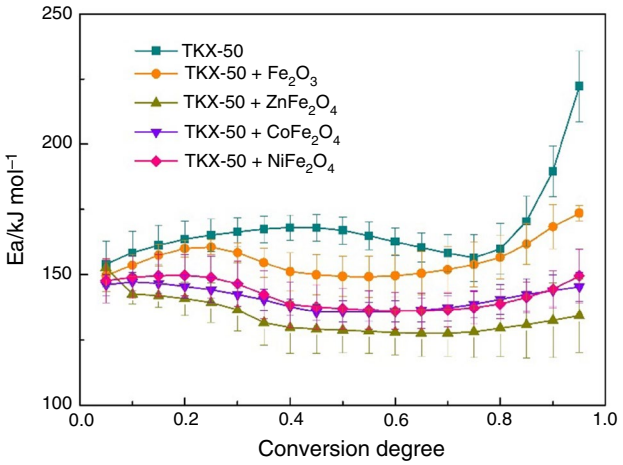

Fig. 7 Activation energy of TKX-50 thermal decomposition obtained from DSC data by iso-conversional Flynn–Wall–Ozawa method

by iteration Kissinger method are in good agreement with the results of iteration Ozawa method. The average activation energies and the error bars of TKX-50 were calculated using iso-conversional methods, and the results are shown in Table 2. As shown in Table 2, the activation energy calculated by multi-kinetic methods is very close and in good agreement with the previous studies, which showed the reliability of the results. In bimetallic iron oxide, $ZnFe_2O_4$ is an efficient combustion catalyst for solid propellant containing TKX-50, which has excellent effect of reducing activation energy and decomposition peak temperature of TKX-50.

Mechanism analysis

The reduction of the decomposition peak temperature and activation energies confirmed the catalytic effects of MFe_2O_4 (M = Ni, Zn and Co) for TKX-50 thermal decomposition. The catalytic effect of MFe_2O_4 (M = Ni, Zn and Co) for thermal decomposition of TKX-50 can be attributed to the reduction of activation energies of TKX-50. Among various catalysts used, $CoFe_2O_4$ has the best catalytic activity for thermal decomposition of TKX-50 which can significantly reduce the decomposition peak temperature and activation energy of TKX-50. The excellent catalytic activities of MFe_2O_4 (M = Ni, Zn, Co) are closely related to its electronic structures, grain size and particle size [33]. The excellent catalytic activity of $ZnFe_2O_4$ can be also attributed to the synergistic interaction between Co and Fe, which is beneficial for the thermal decomposition of TKX-50 [34].

Table 1 Kinetic parameters calculated using iso-conversional Flynn–Wall–Ozawa method

α	TKX-50		TKX-50 + Fe_2O_3		TKX-50 + $ZnFe_2O_4$		TKX-50 + $CoFe_2O_4$		TKX-50 + $NiFe_2O_4$	
	E_a/kJ mol^{-1}	r	E_a/kJ mol^{-1}	r	E_a/kJ mol^{-1}	r	E_a/kJ mol^{-1}	r	E_a/kJ mol^{-1}	r
0.05	154.05 ± 8.7	0.996	149.64 ± 6.2	0.998	152.58 ± 2.4	0.999	146.0 ± 4.0	0.999	147.67 ± 8.5	0.996
0.1	158.38 ± 8.1	0.997	153.57 ± 4.2	0.999	142.46 ± 3.6	0.999	147.17 ± 3.6	0.999	148.98 ± 8.2	0.996
0.15	161.31 ± 7.5	0.997	157.43 ± 4.2	0.999	141.92 ± 4.5	0.998	146.59 ± 3.9	0.999	149.56 ± 8.0	0.997
0.2	163.66 ± 6.9	0.998	159.98 ± 3.3	0.999	140.72 ± 6.4	0.997	145.39 ± 4.5	0.999	149.69 ± 7.9	0.997
0.25	165.14 ± 6.2	0.998	160.54 ± 3.0	0.999	139.29 ± 7.5	0.997	144.05 ± 4.8	0.998	148.91 ± 8.1	0.997
0.3	166.31 ± 5.5	0.998	158.40 ± 3.9	0.999	136.51 ± 8.0	0.996	142.3 ± 4.6	0.998	146.48 ± 8.7	0.997
0.35	167.39 ± 5.1	0.999	154.61 ± 5.6	0.998	131.70 ± 8.8	0.995	140.33 ± 4.0	0.999	142.29 ± 9.0	0.995
0.4	168.03 ± 4.9	0.999	151.12 ± 7.3	0.997	129.81 ± 9.9	0.994	137.64 ± 3.1	0.999	138.52 ± 8.7	0.996
0.45	167.92 ± 5.1	0.999	149.95 ± 7.7	0.987	129.29 ± 9.4	0.994	135.63 ± 2.9	0.999	137.58 ± 8.4	0.996
0.5	166.88 ± 5.3	0.998	149.34 ± 7.7	0.997	128.84 ± 8.8	0.995	135.94 ± 4.0	0.999	136.95 ± 7.8	0.996
0.55	164.92 ± 5.3	0.998	149.16 ± 7.9	0.997	128.42 ± 8.6	0.995	135.68 ± 3.6	0.999	136.43 ± 7.3	0.997
0.6	162.58 ± 5.3	0.998	149.57 ± 8.2	0.997	128.02 ± 8.6	0.995	135.94 ± 4.0	0.999	136.12 ± 6.9	0.997
0.65	160.35 ± 5.6	0.998	150.46 ± 8.4	0.996	127.69 ± 8.9	0.995	136.36 ± 4.4	0.998	136.10 ± 6.6	0.997
0.7	158.22 ± 7.2	0.997	151.91 ± 8.7	0.996	127.67 ± 8.9	0.994	137.17 ± 4.8	0.998	136.46 ± 6.4	0.997
0.75	156.40 ± 9.0	0.996	153.82 ± 8.6	0.996	128.25 ± 10.0	0.993	138.57 ± 5.2	0.998	137.25 ± 6.1	0.998
0.8	159.90 ± 9.8	0.996	156.57 ± 8.3	0.997	129.58 ± 11.0	0.992	140.50 ± 5.7	0.998	138.74 ± 5.6	0.998
0.85	170.45 ± 9.6	0.996	161.73 ± 7.9	0.997	130.90 ± 12.9	0.990	142.30 ± 6.2	0.998	141.13 ± 5.9	0.998
0.9	189.63 ± 9.8	0.997	168.32 ± 8.4	0.997	132.54 ± 14.3	0.988	143.78 ± 6.1	0.998	144.36 ± 7.0	0.997
0.95	222.18 ± 13.5	0.996	173.60 ± 2.9	0.959	134.35 ± 14.0	0.989	145.29 ± 5.5	0 .998	149.48 ± 10.3	0.995

Table 2 Kinetic parameters of TKX-50 obtained using the DSC data

Materials	Equations	Conversion degree	E_a	References
TKX-50	Flynn–Wall–Ozawa	0.3–0.8	163.54 ± 4.0	–
	Iteration Kissinger		162.15 ± 2.5	
	Iteration Ozawa		162.37 ± 2.3	
	Average value		162.69 ± 0.7	
TKX-50 + Fe_2O_3	Flynn–Wall–Ozawa		152.27 ± 3.0	
	Iteration Kissinger		150.67 ± 3.1	
	Iteration Ozawa		151.06 ± 2.9	
	Average value		151.33 ± 0.8	
TKX-50 + $ZnFe_2O_3$	Flynn–Wall–Ozawa		129.61 ± 2.4	
	Iteration Kissinger		128.29 ± 1.2	
	Iteration Ozawa		129.62 ± .1.1	
	Average value		129.17 ± 0.7	
TKX-50 + $CoFe_2O_3$	Flynn–Wall–Ozawa		137.79 ± 2.2	
	Iteration Kissinger		136.23 ± 2.3	
	Iteration Ozawa		137.19 ± 2.2	
	Average value		137.07 ± 0.7	
TKX-50 + $NiFe_2O_3$	Flynn–Wall–Ozawa		138.45 ± 1.7	
	Iteration Kissinger		137.43 ± 3.4	
	Iteration Ozawa		138.46 ± 3.2	
	Average value		138.11 ± 0.3	
TKX-50	Friedman	0.1–0.5	176 ± 8	[17]
TKX-50	Vyazovkin	0.1–0.5	176 ± 8	[17]
TKX-50	Kissinger	–	166.9	[9]

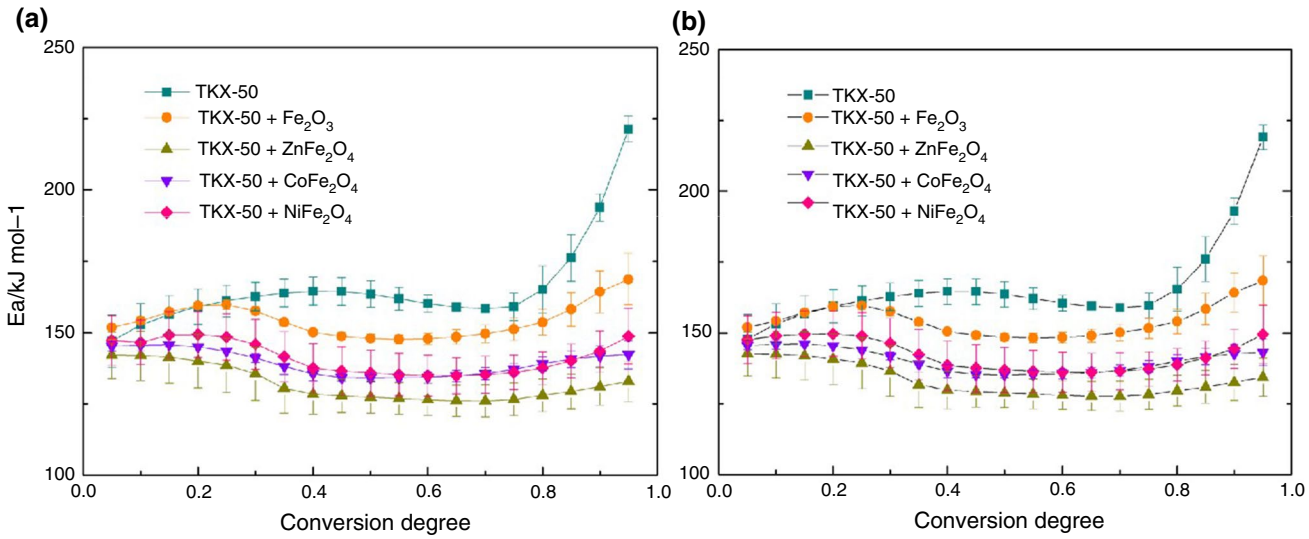

Fig. 8 Activation energy of TKX-50 thermal decomposition obtained from DSC data by nonlinear iso-conversional. **a** Iteration Kissinger method; **b** iteration Ozawa method

Conclusions

The MFe_2O_4 (M = Ni, Zn and Co), which exhibit hollow structure with particle size about 70, 360 and 220 nm, were successfully fabricated via the facile one-pot solvothermal method. DSC and TG-DTG results indicated that the bimetallic iron oxides could effectively promote the thermal decomposition of TKX-50. Besides, the kinetic parameters

of TKX-50 were calculated using multi-methods. The $ZnFe_2O_4$ and $CoFe_2O_4$ possess the better catalytic activity for TKX-50 thermal decomposition compared with $NiFe_2O_4$ and Fe_2O_3. After being mixed with $ZnFe_2O_4$ and $CoFe_2O_4$, the high thermal decomposition peak temperatures of TKX-50 were reduced by 47.0 and 51.2 °C in comparison with the pristine TKX-50 at 10 °C min^{-1}. Besides, the activation energies of TKX-50 ($\alpha = 0.3$–0.8) were decreased by 33.52 and 25.62 in comparison with the pristine TKX-50. Combined with the results of DSC and kinetic parameters, $ZnFe_2O_4$ owns excellent catalytic activity on the thermal decomposition of TKX-50, which can act as an efficient combustion catalyst of solid propellant containing TKX-50. The excellent catalytic performance of $ZnFe_2O_4$ can be attributed to the synergistic effects between Fe and Co, which are beneficial for the fracture of TKX-50.

Acknowledgements The financial support by the National Natural Science Foundation of China (Grant Nos. 21173163 and 21503163) is gratefully acknowledged.

References

1. Tunnell R, Dale R, King I, Tod D. Using thermal methods to understand the interactions between a rocket propellant and igniter material. J Therm Anal Calorim. 2018;131(1):379–95.
2. Trache D, Tarchoun AF. Stabilizers for nitrate ester-based energetic materials and their mechanism of action: a state-of-the-art review. J Mater Sci. 2017;53(1):100–23.
3. Yan Q-L, Yang Z, Zhang X, Lyu J, He W, Huang S, Liu P, Zhang C, Zhang Q, He G, Nie F. High density assembling of energetic molecules under constraint of defected 2D materials. J Mater Chem A. 2019;7:17806–14.
4. Liu L, Li J, Zhang L, Tian S. Effects of magnesium-based hydrogen storage materials on the thermal decomposition, burning rate, and explosive heat of ammonium perchlorate-based composite solid propellant. J Hazard Mater. 2018;342:477–81.
5. Li Y, Huang H, Shi Y, Yang J, Pan R, Lin X. Potassium nitraminofurazan derivatives: potential green primary explosives with high energy and comparable low friction sensitivities. Chem Eur J. 2017;23(30):7353–60.
6. Wu Q, Zhu W, Xiao H. A new design strategy for high-energy low-sensitivity explosives: combining oxygen balance equal to zero, a combination of nitro and amino groups, and *N*-oxide in one molecule of 1-amino-5-nitrotetrazole-3*N*-oxide. Journal of Materials Chemistry A. 2017;2(32):13006.
7. Trache D, Tarchoun AF, Chelouche S, Khimeche K. New insights on the compatibility of nitrocellulose with aniline-based compounds. Propellants Explos Pyrotech. 2019;44:970–9.
8. Zhang X-Q, Yuan J-N, Selvaraj G, Ji G-F, Chen X-R, Wei D-Q. Towards the low-sensitive and high-energetic co-crystal explosive CL-20/TNT: from intermolecular interactions to structures and properties. Phys Chem Chem Phys. 2018;20(25):17253–61.
9. Sinditskii VP, Filatov SA, Kolesov VI, Kapranov KO, Asachenko AF, Nechaev MS, Shishov NI. Combustion behavior and physicochemical properties of dihydroxylammonium 5,5′-bistetrazole-1,1′-diolate (TKX-50). Thermochim Acta. 2015;614:85–92.
10. Chelouche S, Trache D, Tarchoun AF, Abdelaziz A, Khimeche K, Mezroua A. Organic eutectic mixture as efficient stabilizer for nitrocellulose: kinetic modeling and stability assessment. Thermochim Acta. 2019. https://doi.org/10.1016/j.tca.2019.01.015.
11. Trache D, Maggi F, Palmucci I, DeLuca LT. Thermal behavior and decomposition kinetics of composite solid propellants in the presence of amide burning rate suppressants. J Therm Anal Calorim. 2018;132(3):1601–15.
12. Trache D, Tarchoun AF. Analytical methods for stability assessment of nitrate esters-based propellants. Crit Rev Anal Chem. 2019;49:1–24.
13. Trache D, Khimeche K, Mezroua A, Benziane M. Physicochemical properties of microcrystalline nitrocellulose from Alfa grass fibres and its thermal stability. J Therm Anal Calorim. 2016;124(3):1485–96.
14. Mezroua A, Khimeche K, Lefebvre MH, Benziane M, Trache D. The influence of porosity of ammonium perchlorate (AP) on the thermomechanical and thermal properties of the AP/polyvinylchloride (PVC) composite propellants. J Therm Anal Calorim. 2013;116(1):279–86.
15. Trache D. Comments on "thermal degradation behavior of hypochlorite-oxidized starch nanocrystals under different oxidized levels". Carbohydr Polym. 2016;151:535–7.
16. Tarchoun AF, Trache D, Klapötke TM, Chelouche S, Derradji M, Bessa W, Mezroua A. *oceanica* brown algae: synthesis, characterization, and kinetic modeling. Macromol Chem Phys. 2019. https://doi.org/10.1002/macp.201900358.
17. Muravyev NV, Monogarov KA, Asachenko AF, Nechaev MS, Ananyev IV, Fomenkov IV, Pivkina AN. Pursuing reliable thermal analysis techniques for energetic materials: decomposition kinetics and thermal stability of dihydroxylammonium 5,5′-bistetrazole-1,1′-diolate (TKX-50). Phys Chem Chem Phys. 2017;19(1):436–49.
18. Chen S-W, He W, Luo C-J, An T, Chen J, Yang Y, Liu P-J, Yan Q-L. Thermal behavior of graphene oxide and its stabilization effects on transition metal complexes of triaminoguanidine. J Hazard Mater. 2019;368:404–11.
19. Zhang J, Xue B, Rao G, Chen L, Chen W. Thermal decomposition characteristic and kinetics of DINA. J Therm Anal Calorim. 2017;133(1):727–35.
20. Pourmortazavi SM, Mirzajani V, Farhadi K. Thermal behavior and thermokinetic of double-base propellant catalyzed with magnesium oxide nanoparticles. J Therm Anal Calorim. 2018;3:1–12.
21. Zhang J-Q, Liu R, Ji T-Z, Ren J-C, Guo Q, Wang B-Z, Hu R-Z. Thermal behavior and thermal safety of 6b-nitrohexahydro-2*H*-1,3,5-trioxacyclopenta[cd]-pentalene-2,4,6-triyltrinitrate. RSC Adv. 2017;7(49):30747–54.
22. Chen X, Zhang C, Bai Y, Guo Z, Yao Y, Song J, Ma H. Synthesis, crystal structure and thermal properties of an unsymmetrical 1,2,4,5-tetrazine energetic derivative. Acta Crystallogr Sect C Struct Chem. 2018;74(6):666–72.
23. Zhang M, Zhao F, Yang Y, Zhang J, Li N, Gao H. Effect of rGO–Fe_2O_3 nanocomposites fabricated in different solvents on the thermal decomposition properties of ammonium perchlorate. CrystEngComm. 2018;20:7010–9.
24. Zhang M, Zhao F, Yang Y, Li H, Zhang J, Ma W, Gao H, Li N. Shape-dependent catalytic activity of nano-Fe_2O_3 on the thermal decomposition of TKX-50. Acta Phys Chim Sin. 2019;35(X):0001–9.
25. Trache D, Abdelaziz A, Siouani B. A simple and linear isoconversional method to determine the pre-exponential factors and the mathematical reaction mechanism functions. J Therm Anal Calorim. 2016;128(1):335–48.

26. Fu Y, Wang X. Magnetically separable $ZnFe_2O_4$–graphene catalyst and its high photocatalytic performance under visible light irradiation. Ind Eng Chem Res. 2011;50(12):7210–8.
27. Zong M, Huang Y, Wu H, Zhao Y, Wang Q, Sun X. One-pot hydrothermal synthesis of RGO/$CoFe_2O_4$ composite and its excellent microwave absorption properties. Mater Lett. 2014;114:52–5.
28. Huang S, Xu Y, Xie M, Xu H, He M, Xia J, Li H. Synthesis of magnetic $CoFe_2O_4$/g-C_3N_4 composite and its enhancement of photocatalytic ability under visible-light. Colloids Surf A Physicochem Eng Asp. 2015;478:71–80.
29. Zong M, Huang Y, Ding X, Zhang N, Qu C, Wang Y. One-step hydrothermal synthesis and microwave electromagnetic properties of RGO/$NiFe_2O_4$ composite. Ceram Int. 2014;40(5):6821–8.
30. Sun L, Shao R, Tang L, Chen Z. Synthesis of $ZnFe_2O_4$/ZnO nanocomposites immobilized on graphene with enhanced photocatalytic activity under solar light irradiation. J Alloys Compd. 2013;564:55–62.
31. Wang J, Chen S, Yao Q, Jin S, Zhao S, Yu Z, Shu Q. Preparation, characterization, thermal evaluation and sensitivities of TKX-50/GO composite. Propellants Explos Pyrotech. 2017;42(9):1104–10.
32. Jia J, Liu Y, Huang S, Xu J, Li S, Zhang H, Cao X. Crystal structure transformation and step-by-step thermal decomposition behavior of dihydroxylammonium 5,5′-bistetrazole-1,1′-diolate. RSC Adv. 2017;7(77):49105–13.
33. García Rodenas LA, Blesa MA, Morando PJ. Reactivity of metal oxides: thermal and photochemical dissolution of MO and MFe_2O_4 (M = Ni Co, Zn). J Solid State Chem. 2008;181(9):2350–8.
34. Chen S, Zhang H, Wu L, Zhao Y, Huang C, Ge M, Liu Z. Controllable synthesis of supported Cu–M (M = Pt, Pd, Ru, Rh) bimetal nanocatalysts and their catalytic performances. J Mater Chem. 2012;22(18):9117.